PAPER

Check for updates

Nanoscale NiCu electrocatalyst for the hydrogen evolution reaction†

Tatiana Straistari,[a,b] Nuria Romero, [iD] [a,b] Jérôme Esvan,[d] Marcos Gil-Sepulcre,[e] Catherine Amiens, [iD] [a,b] Olaf Rüdiger, [iD] [e] Serena DeBeer, [iD] [e] Sara Cavaliere [iD] [c] and Karine Philippot [iD] *[a,b]

A molecular chemistry synthesis in solution under mild conditions provided a homogeneous nanometric NiCu nanomaterial stabilized by *n*-octysilane. The in-depth structural characterization by state-of-the-art techniques provided evidence for the formation of small nanoparticles of *ca.* 4.1 nm in size with an alloy-type structure. This nanomaterial was then easily deposited onto two different carbon supports, Vulcan and Ketjenblack, by impregnation. The electrocatalytic properties of both unsupported and supported NiCu nanomaterials have been investigated for their activity towards the hydrogen evolution reaction (HER) in alkaline conditions. The electrocatalytic properties indicate the advantageous addition of Cu to Ni as boosted HER performance and stability were observed. Also, the carbon-supported NiCu electrocatalysts presented higher performances as the result of increased conductivity and stabilization effects. Finally, an XPS study suggests that the *n*-octylsilane present at the surface of the NiCu nanoparticles may also intervene in their stabilisation under electrocatalytic conditions. The interest of developing synthesis protocols based on solution chemistry to have structurally controlled nanoscale materials in terms of size, composition, chemical order and surface state, criteria which can strongly influence the catalytic performances, is thus demonstrated in this work.

Introduction

The extensive use of fossil resources for energy generation which reflects the growing global demand in energy, induces an increasing impact on the climate, leading to frequent and diverse environmental crises.[1] Limiting this phenomenon requires new energy sources or fuels that must meet certain criteria, including high calorific potential, minimal pollution during conversion, and economic viability in terms of production cost. While hydrogen[2] appears to be a promising candidate given that it meets almost all of the criteria identified,[3] further progress is still needed to extend its use as an energy carrier, in particular to address its low-carbon footprint production.

Hydrogen is produced by different processes,[4,5] among which water electrolysis is the most sustainable. Within the field of electrochemistry and electrocatalysis, the hydrogen evolution reaction (HER) stands out as a highly studied reaction. Several technologies are being explored to carry out water electrolysis,[6] but only a few are commercially available: alkaline proton exchange membrane (PEM) and solid oxide water electrolysis. PEM electrolysis offers several advantages, including lower operating costs, higher efficiency, and greater flexibility to cope with fluctuations in power demand. However, commercial devices use rare and expensive metals in the cathode and anode, and are limited to acidic media. The replacement of scarce and costly metals by Earth-abundant first row d-metals is challenged by their poor stability in acidic media. A way to overcome this limitation could be the development of the anion exchange membrane (AEM) water electrolysis technology.[7,8] One requirement to bring this technology to the market is the development of electrodes based on non-noble metals that are sufficiently efficient and stable in alkaline media.

Nickel-based materials attract attention for their electrocatalytic activity and stability in alkaline conditions which, together with their low cost, makes them suitable candidates

[a]CNRS, LCC (Laboratoire de Chimie de Coordination), 205 route de Narbonne, BP44099, F-31077 Toulouse Cedex 4, France. E-mail: karine.philippot@lcc-toulouse.fr

[b]Université de Toulouse, UPS, INPT, Toulouse, France

[c]ICGM, University of Montpellier, CNRS, ENSCM, 1919, route de Mende, 34293 Montpellier Cedex 5, France

[d]CIRIMAT, Université de Toulouse, CNRS-INPT-UPS, 4 Allée Emile Monso, BP 44362 31030 Toulouse, France

[e]Max Planck Institute for Bioinorganic Chemistry, Stiftstrasse 34-36, D-45470 Mülheim an der Ruhr, Germany

for electrolysis applications compared with other d-metals. One strategy to improve the performance of Ni-based electrodes is to develop Ni alloys with another non-noble metal. Cost set aside, the significance of incorporating a non-noble d-metal also lies in their reduced affinity for the formation of hydrides, which can favour the desorption of hydrogen.[9]

Composite electrodes combining Ni and Cu have shown high electrocatalytic activity for the HER, indicating that the addition of Cu can boost the properties of Ni-based electrodes. Actually, NiCu alloys present a synergistic effect due to the modification of the electronic structure of Ni by Cu,[10] which facilitates the adsorption and desorption of hydrogen atoms. Development of Ni and Cu composite materials to afford electrocatalysts of improved effectiveness and longevity for hydrogen production is thus a topic of high interest. Several studies describe the preparation of NiCu alloys, with a focus on their structure and morphology which can enhance their electrocatalytic performance. Indeed, nanostructuring has a remarkable advantage for applications in catalysis due to the increased surface to volume ratio, which allows maximization of the surface exposed and the number of active sites, thus reducing the amount of material needed for a given reaction, including the production of hydrogen.[11] The crystalline structures reported for the NiCu system vary from a homogeneous composition where the metals are uniformly distributed[8] to mixtures of segregated islands of the two metals. Electrochemical deposition[12,13] is a widely used method to produce three-dimensional NiCu nanostructures.[14] It allowed the formation of porous materials with various morphologies as foam-like or cauliflower-like.[15] Chemical reduction processes have been also developed to produce NiCu materials. Hence, the reduction of nickel nitrate and copper sulfate with sodium borohydride resulted in materials made of agglomerated nanosheets of NiCu and NiCu oxide alloys.[16] Calcination of nickel and copper acetates at $T > 200$ °C under a hydrogen atmosphere generated a material with a heterogeneous distribution of the two metals.[13] Spherical nanoparticles (NPs) of *ca.* 20 nm in diameter of a NiCu solid solution were obtained by a reduction method.[17] A scalable one-step hydrothermal approach with the assistance of protecting ligands ensured an uniform distribution of Ni and Cu within NiCu solid solution monoliths.[18] The electrocatalytic functions of the NiCu nanoalloys were experimentally and theoretically correlated with the composition-dependent local structural distortion of the bimetallic lattice at the nanoparticle surfaces. Interestingly, carbon-supported alloyed NiCu nanoparticles exhibited multiple catalytic properties, for hydrogen evolution (HER), oxygen reduction (ORR), and oxygen evolution (OER) reactions.[17,19] All these studies highlighted the versatility and potential of NiCu alloys in electrocatalytic applications, but also the need to optimize their synthesis to boost their electroactivity and stability.

Among solution chemistry methods the organometallic approach has proven to be effective for the synthesis of small NPs of various metals, whose size and composition are well-controlled, leading to promising results in the field of catalysis, particularly with regard to HER.[20] Previous results emphasized the relevance of the choice of the metal precursors and stabilizers for the NP synthesis as they can influence their catalytic properties.[21–23]

In this work we report the design of a nanostructured electrocatalyst based on small NiCu NPs capped with *n*-octylsilane for the HER in basic media. The synthesis of this novel NiCu HER electrocatalyst was performed using an organometallic approach. Complementary characterization techniques allowed us to define the structural properties of the nanomaterial. HER activity of **NiCu NPs** was evaluated using a rotating disk electrode (RDE) in comparison with monometallic **Ni NPs**. The **NiCu NPs** supported on Vulcan carbon (C-V) and Ketjenblack carbon (C-K) were characterized.

Results and discussion

Synthesis and characterization

Bimetallic NiCu nanoparticles (**NiCu NPs**) were reproducibly synthesized by using as metal sources the $[Ni(COD)_2]$ (COD = 1,5 cyclooctadiene) and $[Cu(i\text{-butyrate})_2]$ (i-butyrate = $(CH_3)_2CHCOO^-$) complexes in a Ni : Cu ratio of 1 : 1 (Scheme 1). These two precursors were dissolved together in toluene, into a Fisher–Porter reactor, in the presence of *n*-octylsilane as a stabilizer (*n*-octylsilane : metal ratio of 1 : 1). The 1 : 1 ratio of *n*-octylsilane to metal precursors was inspired from a previous work.[24] The reactor was then pressurized with 3 bar of hydrogen under vigorous stirring at room temperature (r.t.) for 10 min before plunging in a pre-heated oil bath at 100 °C for 24 h. Cooling to room temperature (r.t.) and depressurization allowed to recover the colloidal suspension, from which a black solid could be precipitated by slow addition of pentane. The Ni and Cu contents were ascertained by ICP-AES analysis (see Table S1 in the ESI†), indicating a Ni : Cu atomic ratio close to 1.

The decomposition of the nickel and copper precursors separately, in the presence of *n*-octylsilane as a stabilizer and under the same conditions as for the **NiCu NPs**, was also performed to prepare monometallic Ni and Cu NPs for comparison purposes. In the case of nickel, the nanomaterial obtained aligned well with previous results in the literature, presenting Ni NPs of *ca.* 1.3 (0.1) nm as observed by TEM.[25] Upon hydrogenation of the copper precursor, the formation of a metallic agglomerate rather than dispersed nanoparticles was observed, that is also consistent with findings from earlier studies.[26]

Transmission electron microscopy (TEM) and high-resolution (HR) high-angle annular dark-field (HAADF) scanning transmission electron microscopy (STEM) coupled with energy-dispersive X-ray spectroscopy (EDX) images of the **NiCu NPs** are presented in Fig. 1 (see also Fig. S1, S2 and S4 in the ESI†). The micrographs showed well-dispersed NPs with a mean diameter of *ca.* 4.1 (0.4) nm that are crystalline and contain both nickel and copper, thus confirming the formation of bimetallic **NiCu NPs**. In addition, HR-STEM-HAADF-EDX in-line analysis revealed a homogeneous distribution between nickel and copper within the
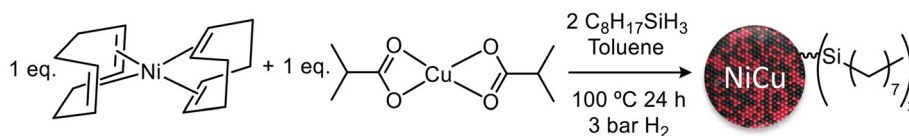
Scheme 1 Synthesis of **NiCu NPs** by hydrogenolysis of [Ni(COD)$_2$] and [Cu(i-butyrate)$_2$] in the presence of *n*-octylsilane as a stabilizer.
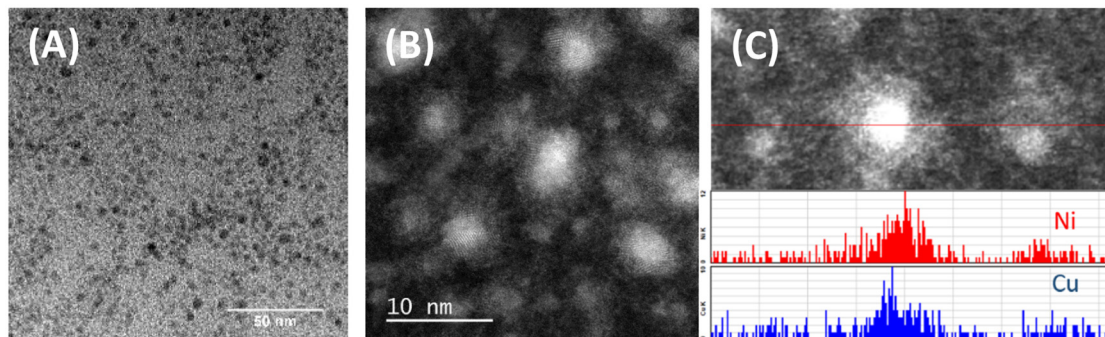

Fig. 1 TEM (A), HR-HAADF-STEM (B) and HR-HAADF-STEM-EDX in line of one nanoparticle (red for nickel; blue for copper) (C) of **NiCu NPs** (d_m = 4.1(0.4) nm).

NPs, in better agreement with an alloy than with a core–shell structure (Fig. 1c). This hypothesis was further confirmed by powder-X-ray diffraction (p-XRD) analysis of the carbon-supported **NiCu NPs** (*vide infra*).

The Fourier transform infrared (FTIR) spectrum of the fresh **NiCu NPs** was recorded (in ATR mode) in order to probe the coordination of the *n*-octylsilane at the NP surface (Fig. 2). Characteristic stretching bands ($\nu_{C–H}$ vibrations) of aliphatic –CH$_2$ and –CH$_3$ groups were clearly observed between 2800–3000 cm^{-1}.[27] Interestingly, the absence of a characteristic peak for the Si–H groups, which was expected around 2145 cm^{-1} in comparison with the pure *n*-octylsilane,

suggested the breaking of the Si–H bonds and the coordination of silyl groups to the metal atoms at the NP surface.[28] The presence of M–Si bonds was further confirmed by X-Ray Photoelectron Spectroscopy (XPS) (*vide infra*).[27]

NiCu NPs were deposited onto two different carbon supports, Vulcan carbon (**C-V**) and Ketjenblack carbon (**C-K**), to afford two different carbon-supported NiCu nanomaterials, **NiCu/C-V** and **NiCu/C-K**, respectively. The deposition was performed by mixing a suspension of carbon and a fresh **NiCu NPs** colloidal suspension, both in toluene. This operation was done in a way to achieve a total metal weight% of *ca.* 50% on the carbon supports. TEM analysis of the **NiCu/C-V** and **NiCu/C-K** materials confirmed the efficient and homogeneous immobilization of the **NiCu NPs** onto both carbon supports (Fig. S5†). The NP size measurement led to a similar value for the two nanomaterials of *ca.* 4.1 (0.6) nm for **NiCu/C-K** and *ca.* 4.3 (0.6) nm for **NiCu/C-V**, respectively. These results clearly indicate that the deposition process did not provoke a change in the **NiCu NP** size. The metal weight% was determined by ICP-AES, namely 25.4% of Ni and 27.4% of Cu for **NiCu/C-K**, and 21.8% of Ni and 24.3% of Cu for **NiCu/C-V**, respectively (see Table S1†), close to the targeted total metal content (50%).

The p-XRD diffractograms recorded on the unsupported **NiCu NPs** and the two carbon-supported NiCu counterparts are presented in Fig. 3. For comparison, reference XRD patterns for monometallic Cu and Ni as well as 1 : 1 NiCu alloy are also provided. For the three materials, the results clearly show three similar patterns with characteristic peaks at $X°$, $Y°$ and $Z°$ (44°, 51° and 75°) that fit well with the values of the (111), (020) and (022) lattice planes of the fcc crystalline structure for a NiCu alloy. As expected, similar patterns are observed for **NiCu/C-K** and **NiCu/C-V**.
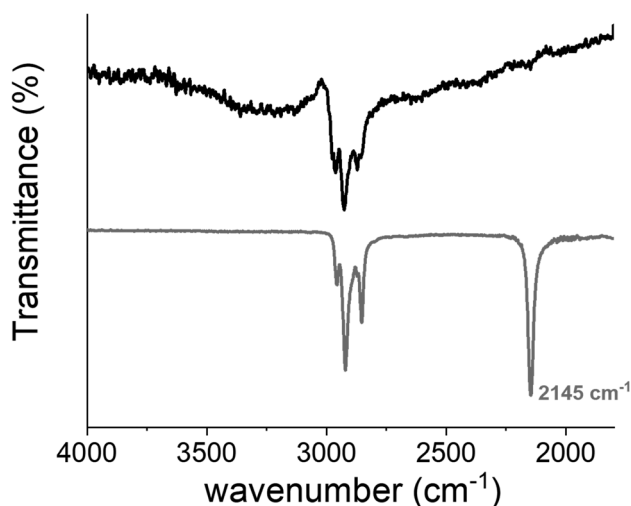

Fig. 2 Infrared spectra of *n*-octylsilane-stabilized **NiCu NPs** (black) and of pure *n*-octylsilane (grey) in the 4000–1750 cm^{-1} region.[27]
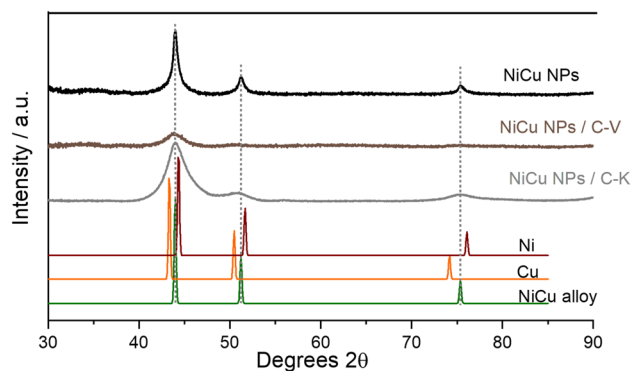
Fig. 3 p-XRD diffractograms of **NiCu NPs**, **NiCu/C-K** and **NiCu/C-V** in comparison with the references of Ni,[29] Cu,[30] and NiCu alloy[31] (vertical grey dots lines are landmarks for overlapping with the NiCu alloy reference green pattern).

The **NiCu NP** surface composition was investigated by XPS. A first XPS analysis was performed on the freshly synthesized **NiCu NPs** to determine the initial metal state. Another XPS analysis was performed on the same batch of **NiCu NPs** after exposure to air for one week because the ink preparation for electrochemical experiments was made in air. The long-range survey spectrum of initial **NiCu NPs** (Fig. S6†) displays Ni, Cu, Si, C and O signals. As illustrated in Fig. 4(A), Ni 2p region shows mainly two oxidation states for Ni, Ni(0) with Ni $2p_{3/2}$ at 852.5 eV, and Ni(II) for the hydroxide form (Ni(OH)$_2$) with Ni $2p_{3/2}$ at 855.9 eV, which is consistent with previous literature values.[32]

From the Cu 2p peak at 932.4 eV (Fig. 4(B)) and the Auger CuL$_3$M$_{4,5}$M$_{4,5}$ peak at 918.6 eV (Fig. 4(C)), the Auger parameter was determined: $\alpha' = 1851$. This value indicates an oxidation state Cu(0)[27,33] for Cu in **NiCu NPs**. The signals observed for oxidized species could arise from rapid oxidation during introduction of the sample into the XPS equipment despite the high caution taken to limit this phenomenon. Deconvolution of the Si 2p signal provides evidences for Si $2p_{3/2}$ and Si $2p_{1/2}$ peaks at 99.0 and 99.6 eV, respectively, which are characteristic of Si in metal silicide bonds[34,35] and two peaks at 101.8 eV and 103.1 eV which could be attributed to Si in O–Si–C and Si–(O)$_4$ chemical environments, respectively (Fig. 4(D)). For the C 1s
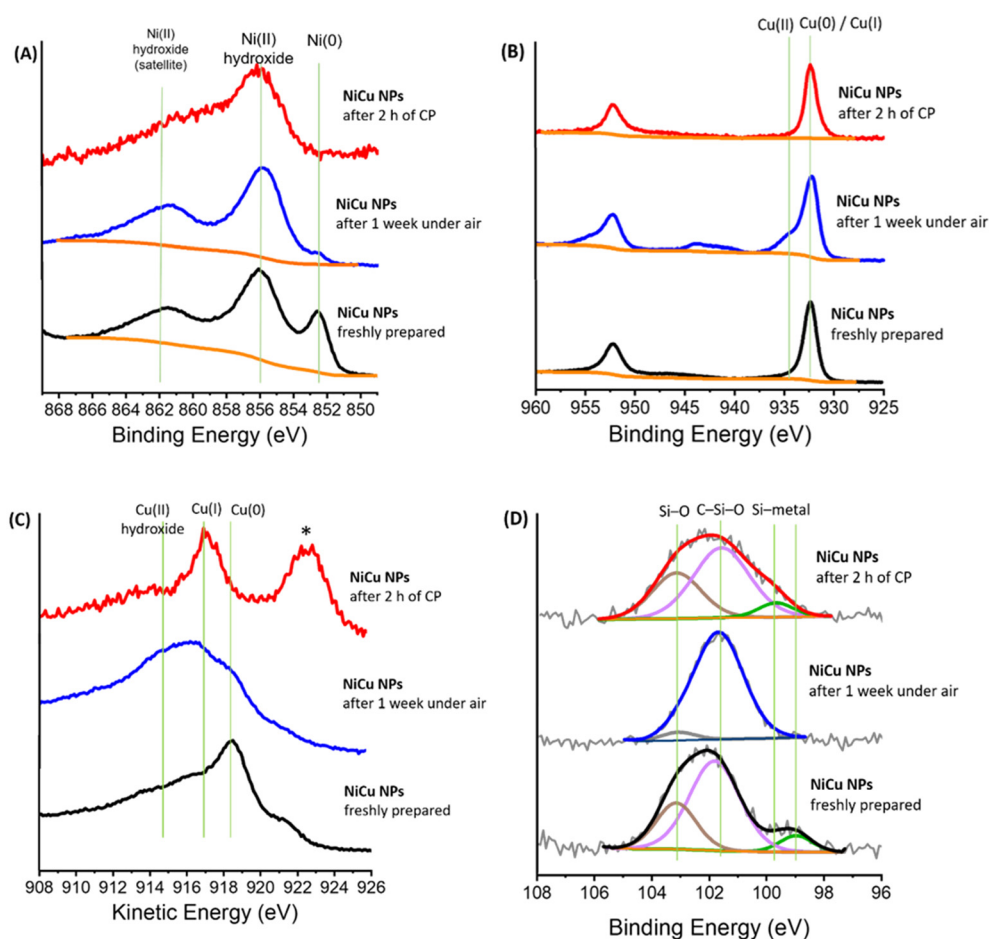

Fig. 4 High-resolution XPS spectra of (A) – Ni 2p, (B) – Cu 2p, (C) – CuLM2 and (D) – Si 2p (with the deconvolution of the signals). For each element: freshly prepared **NiCu NPs** (black), the same **NiCu NPs** exposed to air for a week (blue) and **NiCu NPs** deposited as an ink onto a glassy carbon electrode after 2 h of CP at a potential of −10 mA cm^{-2} in 0.1 M NaOH (red). * – the peaks at 923 eV are due to the Na KLL line.[37]

XPS spectrum (Fig. S7†), the deconvolution of the signal leads to a peak at 284.9 eV that can be assigned to C in aliphatic C–C, C–H or C–Si–O environments, and to two peaks at 286.3 eV and 288.5 eV to C in C–O and O=C–O, respectively.

Prolonged exposure of the **NiCu NPs** in open air led to several changes in the XPS spectrum (Fig. 4; see also Table S2†). The Ni(0)/Ni(hydroxide) ratio decreased to 0.05 *vs.* 0.44 for the freshly prepared **NiCu NPs**, indicating an important oxi/hydroxidation of Ni. For the Cu $2p_{3/2}$ signal, an additional peak is observed at 934.5 eV which shows the presence of Cu(II). In the Si 2p spectrum, the disappearance of the peaks at 99.0 eV (Si $2p_{3/2}$) and 99.6 eV (Si $2p_{1/2}$) is a consequence of the NP oxidation. These results emphasize a discontinuous surface of a metal (nickel/copper) oxide region in the air-exposed **NiCu NPs**. Interestingly, it is reported in the literature that oxide sites may facilitate the water dissociation by significantly lowering the dissociation energy barrier.[9,36]

The electronic structure and coordination environment of the metal atoms in the **NiCu NPs** were further investigated by X-ray absorption spectroscopy (XAS), a technique sensitive to the oxidation state, geometry, and coordination environment of the metal centers. The Ni K-edge and Cu K-edge X-ray absorption near-edge structure (XANES) spectrum of the **NiCu NPs** deviates from what is expected for pure metallic Ni(0) (*ca.* 8333 eV) and Cu(0) (*ca.* 8979 eV). Indeed, the edge shapes and positions indicate the presence of a nickel oxide or hydroxide (Fig. 5A) and of oxidized Cu(I) and/or Cu(II) (Fig. 5C). Fitting of the Ni K-edge XANES for the **NiCu NPs** was performed to roughly estimate the species ratio. Combining the spectra of Ni(0), NiO and Ni(OH)$_2$ with a 1.95 : 1 : 1.6 ratio (Fig. S8A†) yielded a satisfactory fitting. Similar analysis of the Cu K-edge XANES spectrum led to a 3.7 : 3 : 1 ratio of Cu(0), Cu$_2$O and CuO, respectively (Fig. S8B†). Note that, at both Ni- and Cu-edges, fitting the XANES region by using only mixtures of the purely metallic components with a single oxidized form of the metal was not possible, which strongly supports the presence of ternary mixtures. Extended X-ray absorption fine structure (EXAFS) spectroscopy provided additional insights into the coordination environment of the Ni and Cu centers. The R-space spectrum at the Ni K-edge, fitted using the Ni(0)/NiO/Ni(OH)$_2$ model, is shown in Fig. 5B (see also Fig. S9† left). This spectrum is dominated by the contribution from Ni–Ni
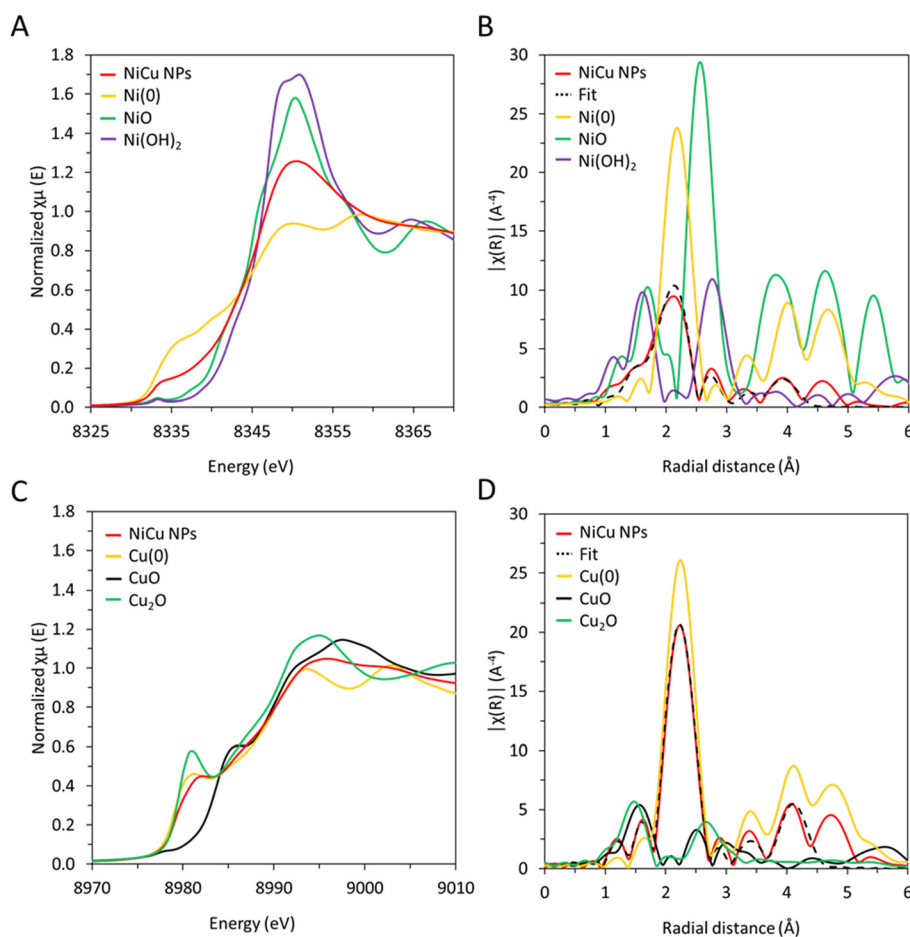

Fig. 5 (Left) Normalized Ni and Cu K-edge XANES spectra of **NiCu NPs** along with Ni(0), NiO, Ni(OH)$_2$ and Cu(0), Cu$_2$O and CuO references (A and C, respectively). (Right) Fourier transforms of the k^3-weighted Ni and Cu EXAFS spectra for **NiCu NPs** along with Ni(0), NiO, Ni(OH)$_2$ and Cu(0), Cu$_2$O and CuO references (B and D, respectively).

scattering vectors in metallic Ni(0) at 2.49 Å, along with two less intense peaks at 2.05 Å and 3.03 Å, attributed to Ni–O and Ni–Ni distances in $NiO/Ni(OH)_2$, respectively (see Table S3†). At the Cu K-edge, the R-space spectrum is characteristic of Cu (0), featuring a strong contribution from the first shell Cu–Cu distances at 2.53 Å and only a minor contribution from Cu–O scattering at approximately 1.91 Å (see Fig. 5D and S9† right). Overall, XAS analysis indicates that the NiCu nanomaterial is mainly formed by $NiO/Ni(OH)_2$ (ca. 65% of Ni species) and Cu (0) (ca. 48% of Cu species) with the presence of ca. 35% of Ni (0) and ca. 52% Cu_2O/CuO. The presence of oxidized Ni and Cu is due to surface oxidation of the **NiCu NPs** when exposed to air during preparation for analysis, conditions which actually correspond to those for the electrocatalysis (vide infra). These X-ray absorption spectroscopy results are consistent with those from XPS analysis (blue curve). The catalyst is thus best described as **NiCu@NiCuO$_x$** NPs.

Electrocatalytic hydrogen evolution reaction (HER) studies

The catalytic activity of the **NiCu NPs**, **NiCu/C-K** and **NiCu/C-V** nanomaterials in HER was evaluated under aqueous alkaline conditions (pH 13–0.1 M NaOH) in a three-electrode electrochemical cell configuration and compared to the HER activity of the monometallic **Ni NPs**. The working electrode was prepared following the protocol detailed in the Experimental section.

The initial polarization curve of the unsupported **NiCu NPs** at t = 0 is presented in Fig. 6 (black line). A change of slope in the current density was observed when scanning towards cathodic potentials, indicating HER catalytic activity, with η_0 = 388 mV and η_{10} = 633 mV which are the onset (at the change of slope) and benchmarking (at j = −10 mA cm^{-2}) overpotentials, respectively, commonly used descriptors for the electrocatalytic HER. The long-term stability assessment was studied over 24 h by performing a chronopotentiometry (CP) experiment, by applying a current-controlled bulk electrolysis at j = −10 mA cm^{-2} (Fig. 6(B), blue line). At the beginning of the CP experiment, an overpotential decrease was observed, which can be attributed to an activation of the catalyst under electrocatalytic conditions. Upon reducing electrocatalytic conditions.

Then, the potential was found stable and the catalyst exhibited HER activity with η_0 = 60 mV and η_{10} = 273 mV. For a comparative purpose, the polarization curves of **Ni NPs** at t = 0 and after 2 h of CP are shown in the ESI (Fig. S10†) together with those of the unsupported **NiCu NPs**. The **Ni NPs** displayed different overpotentials than those of the **NiCu NPs**: η_0 = 657 mV and η_{10} = 903 mV (freshly prepared **Ni NPs** electrode) vs. η_0 = 388 mV and η_{10} = 633 mV for freshly prepared **NiCu NPs** and η_0 = 476 mV; η_{10} = 753 mV (**Ni NPs** electrode after 2 h of bulk electrolysis) vs. η_0 = 240 mV and η_{10} = 505 mV for **NiCu NPs** after 2 h CP. Even if an activation is noticed after 2 h of CP, the overpotential remains quite high at η_{10} for the monometallic **Ni NPs**. These results indicate that the combination of Cu with Ni led to a more active HER catalyst as the result of cooperative effects, like electronic effects that can induce a lower binding energy of intermediates for instance, as often reported for this and other catalytic reactions.[38–40]

The faradaic efficiency of the **NiCu NPs** towards the formation of H_2 was determined using a two-compartment cell to separate the evolved O_2 and H_2 (see detail in the Experimental part) and a Clark electrode to quantify the H_2 generated during an electrolysis (−10 mA cm^{-2}) vs. the theoretical H_2 amount given by the passed charge (Fig. 7). The experiment, performed for 20 min (Fig. S11†) on the 2 h CP-activated **NiCu NPs**, led to a reproducible faradaic efficiency of 99%. This quantitative result clearly indicates that the HER is the only reaction occurring over the NiCu nanocatalyst.

For evaluating the HER activity of the catalysts, the methodology most commonly referenced is that described by Jaramillo and collaborators.[41] This method involves determining the electrochemically active surface area (ECSA) by relating the double-layer capacitance (C_{DL}) to the specific conductivity (C_s) of the material under the applied electrochemical conditions. In the literature, references to the C_s of bimetallic materials are limited. With the ECSA value we can determine the roughness factor (RF) of the analyzed electrode, see in ESI (Table S4, ESI†). Therefore, to determine the ECSA value, we used the method described by Morozan et al.[42] The ECSA of the freshly prepared **NiCu NPs** in the presence of $K_3[Fe(CN)_6]$ in 0.1 M NaOH was estimated to 13.8×10^{-2} cm^2 (see calcu-
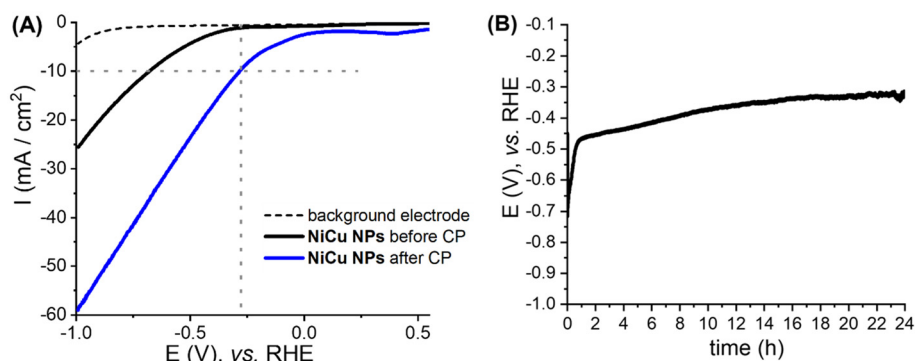

Fig. 6 (A) − LSV of **NiCu NPs** before (black line) and after (blue line) 24 h CP, (B) − CP curve obtained with the **NiCu NPs** electrode in 0.1 M NaOH solution with a constant applied current density (j = −10 mA cm^{-2}).
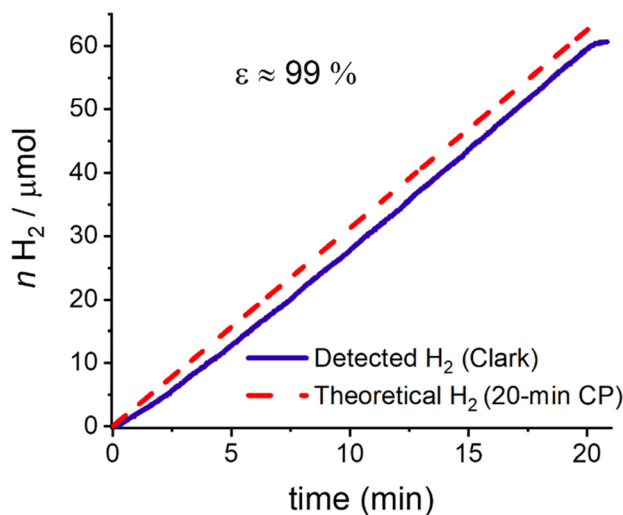
Fig. 7 H$_2$-monitored current-controlled bulk electrolysis of **NiCu NPs** in 0.1 M NaOH solution. Comparison of the theoretical and experimental amount of H$_2$ produced during the 20 min electrolysis.

lation detail in the ESI and Table S4†). The calculated C_{DL} value, determined as in ref. 41, was 6.81 ± 0.25 μF, which aligns with the expected electrochemical characteristics of the surface under investigation and was compared to the ECSA to ensure consistency in measurement. This is a key validation step, as the ECSA value offers a secondary verification metrics that reflects the active surface area of the electrode. In addition to the ECSA correlation, the C_{DL} value was cross-referenced with values reported in previous studies that utilized alternative methods for C_{DL} determination (such as cyclic voltammetry). These studies[42] report values that fall within a comparable range, underscoring that the 6.81 ± 0.25 μF value is both accurate and reproducible across different methodologies. This convergence of C_{DL} values obtained through various methods indicates methodological robustness and consistency of the electrochemical surface properties across different experiments, contributing to the reliability and reproducibility of the C_{DL} value obtained in this study. Such alignment with literature values further strengthens the validity of Jaramillo *et al.*'s methodology for C_{DL} determination in electrochemical analyses. The uncompensated resistance (R) was measured by electrochemical impedance spectroscopy (EIS). Our cell setup (from BioLogic Instruments) gave a R value of ~66 Ω at the potential used for ECSA determination (150 mV *vs.* SCE), in the non-faradaic region.[17,19]

The integrity of the used NiCu nanocatalyst was studied by TEM analysis of the material recovered from the electrode post-catalysis. As seen in the ESI (Fig. S14†), the used catalyst present NPs with morphology and size similar to those of the initial **NiCu NPs**, thus indicating no significant degradation. This result supports the remarkable stability of the NiCu nanocatalyst in the applied electrocatalytic conditions. Moreover, a post-catalytic XPS analysis was performed on a glassy carbon (GC) plate electrode prepared by dropcasting the **NiCu NPs** in

the presence of Nafion polymer to maximize the adherence of the material, which was run under turnover conditions for 2 h, (Fig. S15, ESI†). The aim was to gain information on the catalyst surface composition after exposure to the electrocatalytic conditions. The used electrode was transferred to the XPS equipment under argon flow to avoid possible re-oxidation of the nanomaterial. The initial survey spectrum evidenced the presence of Ni, Cu, Si, C and O signals. As illustrated in the high-resolution Ni 2p XPS spectrum (Fig. 4), it is difficult to extract the chemical environment of Ni because there is an overlap with the Auger signal of fluorine (from the Nafion polymer). The main Ni 2p$_{3/2}$ peak, at 856.3 eV, indicates the presence of Ni(II) hydroxide.[32] The Auger parameter (α' = 1849.5) determined from the Cu 2p peak at 932.4 eV and the Auger CuL$_3$M$_{4,5}$M$_{4,5}$ peak at 917.1 eV (kinetic energy) does not match exactly the value expected for the Cu(0) form but may correspond to a mixture of Cu(0) and Cu(I)[32] in the **NiCu NPs**. The deconvolution of the Si 2p signal evidenced Si 2p$_{3/2}$ (at 99.6 eV) and Si 2p$_{1/2}$ (at 100.2 eV) peaks, that can be assigned to Si involved in metal silicide bonds[34,35] and two Si 2p peaks at 101.6 eV and 103.2 eV attributed to Si atoms in O–Si–C and Si–(O)$_4$ chemical environments, respectively. The deconvolution of the C 1s XPS spectrum (Fig. S7, ESI†), evidenced a peak at 284.5 eV assigned to graphitic carbon,[43] and/or C–Si–O response. The peaks at 285.2 eV, 285.9 eV and 288 eV were assigned to C involved in CH$_x$, C–O, O=C, respectively, and those at 292.3 eV and at 295.5 to C in C–F groups arising from presence of Nafion. Comparison of the XPS spectra of **NiCu NPs** recorded before and after their use to catalyse the HER, allows some hypotheses to be drawn on the nature of the species active in HER. First, no change in the oxidation state of Ni is visible. Indeed, Ni(II) features corresponding to Ni(OH)$_2$ are observed both from the air-exposed sample and after the reduction treatment, suggesting that Ni(II) is the oxidation state of the active species. Second, Cu(II) features are observed on the air-exposed surface which is then reduced to Cu(I) or Cu(0) under catalytic conditions. Third, Si is oxidized upon air exposure to form Si–O bonds whereas the Si–M features are lost, but the reduced state of Si is at least partially restored under catalytic conditions. This suggests the presence of residual *n*-octylsilyl groups at the surface of the **NiCu NPs** under HER conditions, and their key role in the stabilisation of the catalyst, and further rises the question of their influence on the catalytic activity of the **NiCu NPs**.

The electrocatalytic behaviour of the carbon-supported **NiCu NPs** was then studied (Fig. 8). Initial LSV experiments with **NiCu/C-V** (red line) and **NiCu/C-K** (green line) of the freshly prepared electrodes showed η_0 = 338 mV; η_{10} = 450 mV and η_0 = 291 mV; η_{10} = 403 mV, respectively. Then a stability test was carried out over 2 h by performing CP at j = −10 mA cm^{-2}. The CP curves indicate firstly activation and then stabilization of the catalyst at a given potential after a few minutes, for both electrodes (Fig. S16†). Analysis by LSV after the 2 h CP showed a reduction of the benchmarking overpotential to η_0 = 228 mV; η_{10} = 273 mV for **NiCu/C-V** and η_0 = 275 mV; η_{10} = 305 mV for **NiCu/C-K**. As the **NiCu/C-V** and **NiCu/C-K** nano-
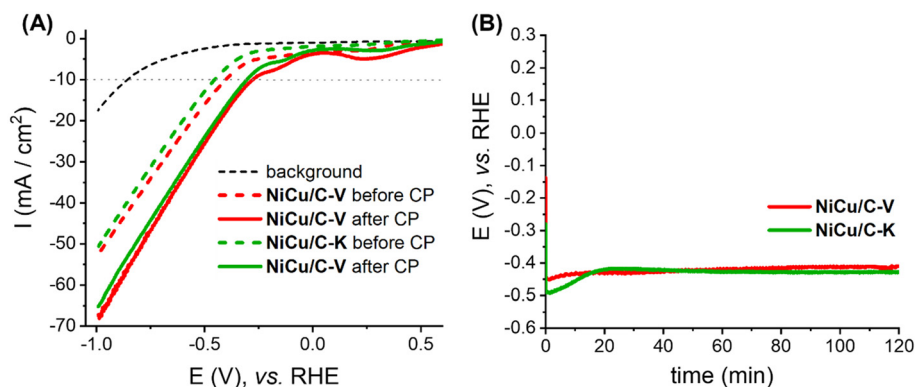
Fig. 8 (A) – LSV of **NiCu/C-V** (red) before (dashed line) and after (solid line) a 2 h CP; **NiCu/C-K** (green) before (dashed line) and after (solid line) a 2 h CP; (B) – CP curves obtained with the **NiCu/C-V** (red) and **NiCu/C-K** (green) electrodes in 0.1 M NaOH solution with a constant applied current density (-10 mA cm^{-2}).

materials are expected to display the same air-sensitivity as their unsupported counterpart, **NiCu NPs**, this observation is again ascribed to the reduction of the oxide shell at the surface of the NPs under turnover conditions. A longer stability test over 18 h was also performed for the **NiCu/C-K** catalyst, with stable potential being observed (Fig. S17†). The stability of the **NiCu/C-K** catalyst was further confirmed by recording the LSV after the 18 h test. Interestingly, the overpotential difference required for activation of **NiCu/C-K** catalyst after 18 h ($\Delta(\eta_{10}) = 179$ mV; difference between the potential fixed at 10 mA cm^{-2} before and after CP in Fig. S17†) was found to be lower than that of the unsupported **NiCu NPs** ($\Delta(\eta_{10}) = 406$ mV; difference between the potential fixed at 10 mA cm^{-2} before and after CP on Fig. 6). This result highlights the boosting effect of the carbon support onto the HER activity of the **NiCu NPs**.

A significant advantage of the carbon-supported NiCu catalysts is thus their shorter activation period. By comparing the chronopotentiometry curves performed at $j = -10$ mA cm^{-2} of the unsupported and supported **NiCu NPs**, we observed that the potential for the carbon-supported **NiCu NPs** was immediately lower and remained stable for 2 h. In contrast, the overpotential for the unsupported **NiCu NPs** decreased continuously during this period (ESI, Fig. S10†). This may be explained by both the increased conductivity and the stabilization effects of the carbon support on the **NiCu NPs**. We can thus conclude that, due to its intrinsic conductivity and metal dispersion properties,[42] the deposition of the **NiCu NPs** onto a carbon support is an effective strategy to enhance the HER catalytic performance and stability.

The Tafel plots derived from the polarization curves (LSV) of the **NiCu NPs**, **NiCu/C-V** and **NiCu/C-K** catalysts were plotted in order to explore the kinetics and mechanistic pathway in the HER (Fig. 8). Several mechanisms are described for conventional heterogeneous catalytic HER with typical figures of merit for each step of these mechanisms.[44] This allows the limiting step to be determined from the Tafel slope and a mechanism to be assigned, when studying a novel catalytic

system. Previously reported Ni-based materials for HER displayed Tafel values around 400 mV dec^{-1}, indicative of a mechanism proceeding through hydroxide intermediates rather than hydrides[45] or a multistep reaction pathway[46] with the formation of the active species as the rate determining step. The three NiCu nanomaterials studied here exhibited unusually high Tafel slope values ($\sim$500–450 mV dec^{-1}) that cannot be ascribed to any rate determining step of any of the classical catalytic pathways (see Fig. S18†). This remarkable behaviour may be due either to the influence of Cu on Ni as previously reported in the literature, or to the **NiCu NP** size or also to the *n*-octylsilane used to synthesize the **NiCu NPs**. With regard to the latter hypothesis, the influence of the *n*-octylsilyl groups in the catalysis may be supported by the "regeneration" of reduced silicon on the surface of the **NiCu NPs** during electrocatalysis, as indicated by XPS data of silicon. This may allow the liberation of active sites while maintaining the stability of the **NiCu NPs** owing to the proximity of reduced silane species.

Conclusion

This work reports the organometallic synthesis of bimetallic **NiCu NPs** using *n*-octylsilane as a stabilizer and their deposition onto two different carbon supports (carbon Vulcan and carbon Ketjenblack) to compare their potential as HER catalysts. The full characterization of the **NiCu NPs** by TEM and p-XRD provided evidence for the formation of small, well-dispersed NPs (4.1 ± 0.4 nm) with a fcc crystalline structure, which matches well with a NiCu alloy. Also, metal–silicide bonds were detected by XPS analysis, formed as the result of the splitting of the Si–H bond when the *n*-octylsilane interacted with the NP surface during their formation. In comparison to monometallic Ni NPs prepared in similar synthesis conditions, the evaluation of the unsupported and carbon-supported NiCu nanocatalysts in HER in 0.1 M NaOH, revealed an efficient electroactivity towards the evolution of hydrogen. After an activation period under reduction conditions at a

current density of $j = -10$ mA cm^{-2}, the unsupported NiCu nanocatalyst presented a lower η_{10} overpotential than mono-metallic Ni catalyst (503 mV *vs.* 753 mV after 2 h of CP at $j = -10$ mA cm^{-2}), thus demonstrating the advantageous combination of Cu and Ni to achieve a higher activity. Furthermore, XPS analysis of the NiCu nanocatalyst recovered after the electrocatalysis turnover evidenced the presence of residual M–Si bonds, so supporting the robustness of the coordination of the *n*-octylsilane at the NiCu nanoparticle surface in the form of *n*-octylsilyl groups, as supported by the XPS data. This strong M–Si interaction probably contributes to the high stability observed for the **NiCu NPs** in the applied HER conditions but it rises also the question of their influence on their catalytic activity. Actually, the regeneration of reduced silicon on the surface of the **NiCu NPs** during electrocatalysis as revealed by XPS studies, makes plausible the liberation of active sites while keeping the stability of the **NiCu NPs** owing to the proximity of reduced silane species.

Interestingly, the carbon-supported **NiCu NPs** needed a shorter activation period to achieve efficient hydrogen evolution with η_{10} overpotentials of 275 mV and 305 mV for **NiCu/C-V** and **NiCu-C-K**, respectively, and showed long-standing stability under turnover conditions (up to 18 h). The lower η_{10} overpotentials achieved with the carbon-supported **NiCu NPs** can be explained by the conductivity of the carbon supports which increases the electrocatalytic performance.

The successful results of this work corroborate the interest of developing nanostructured catalysts for alkaline HER as well as the advantage of using alloy-type bimetallic NPs in which both metals can have cooperative effects to achieve higher electrocatalytic performance. Our results suggest a positive effect of the *n*-octysilane used as a stabilizer for the synthesis of **NiCu NPs**, which seems to contribute to the stability of the CuNi catalyst and perhaps also to its activity, although this question remains open. Deposition on carbon supports also led to improved HER performance of **NiCu NPs** in terms of both activity and stability. Our work thus opens new directions for the development of more stable while performant nanocatalysts for the production of hydrogen using anion exchange membrane water electrolysis technology, which is still an issue to solve.

Experimental part

General information

Most of the chemical operations concerning the synthesis of **NiCu NPs** or characterisation were carried out using standard Schlenk tubes, Fisher–Porter bottle techniques under argon or hydrogen atmosphere or in glovebox under argon atmosphere. High purity Ar and H$_2$ gases were purchased from Air Liquide. The solvents were purchased from Carlo Erba. Toluene and pentane were purified before use by filtration, on adequate columns in a purification apparatus (MBraun). Water content in solvents was determined with a Karl Fisher Coulometer (Metrohm) (target value for use of solvents < 5 ppm). The [Ni

(COD)$_2$] and Cu(iBu)$_2$ complexes were purchased from Strem Chemicals. *N*-Octylsilane was bought from abcr GmbH and the carbon supports (Ketjenblack and Vulcan) from fuel cell store. All chemicals were used as received, except a vacuum treatment to evacuate air.

Synthesis of nanomaterials

NiCu NPs: a dry Fisher–Porter reaction vessel was charged in a glovebox with 47.54 mg of copper(II)i-butyrate (0.2 mmol) and 77 µl of *n*-octylsilane (0.4 mmol) in 40 ml of toluene, giving a turquoise solution. Then, 55 mg bis(cyclooctadiene)nickel(0) (0.2 mmol) were added to the reactor. The resulting solution was pressurized with 3 bar of H$_2$ under vigorous stirring (1000 rpm) and heated to 100 °C overnight in an oil bath. The black resulting solution was then cooled down to room temperature under strong stirring before depressurization of the reactor to evacuate H$_2$. The **NiCu NPs** were precipitated by slow diffusion of pentane in the colloidal NiCu suspension and then washed three times with pentane before drying under argon. 32 mg of black powder is isolated.

Ni NPs: a dry Fisher–Porter reaction vessel was charged in a glovebox with 110 mg of bis(cyclooctadiene)nickel(0) (0.4 mmol) and 77 µl of *n*-octylsilane (0.4 mmol) in 40 ml of toluene. The solution was pressurized with 3 bar of H$_2$ and heated to 100 °C overnight. The workup was carried out as described above leading to 14 mg of a black powder.

Carbon (C–K, C–V)-supported NiCu: to obtain **NiCu/C-K** or **NiCu/C-V** a fresh colloidal suspension of the as-synthesized **NiCu NPs** (obtained from 0.2 mmol copper(II)i-butyrate and 0.2 mmol bis(cyclooctadiene)nickel(0) precursors, and 0.4 mmol of *n*-octylsilane in 40 ml of toluene) was added by cannula over a suspension of 25 mg of carbon – Ketjenblack (C-K) or carbon vulcan (C-V) in 10 ml of toluene in a Schlenk tube under argon. The mixture was then stirred at room temperature for 72 h. After this reaction time, stirring was stopped and the nanomaterial was left to slowly precipitate. The mother solution was removed by filtration with cannula and the resulting carbon material was washed three times with pentane. The last washing solution was completely colourless and transparent. **NiCu/C-K** or **NiCu/C-V** nanomaterials were characterized by TEM, showing a mean size of 4.1 ± 0.6 nm and 4.3 ± 0.6 nm, respectively. The metal content was determined by ICP-AES, giving 25.4% Ni and 27.4% Cu for **NiCu/C-K** and 21.8% Ni and 24.3% Cu for **NiCu/C-V**, respectively.

Characterization methods

Transmission electron microscopy (TEM) and high-resolution transmission electron microscopy (HR-TEM) analyses were performed at the Centre de microcaractérisation Raimond Castaing, CNRS-UAR 3623, Toulouse, on a JEOL JEM 1400 operating at 120 kV with a point resolution of 2.0 Å, and high-angle annular dark-field imaging scanning transmission electron microscopy (HAADF-STEM) on a JEOL JEM-ARM200F Cold FEG operating at 200 kV with a point resolution of >1.9 Å, respectively. Samples were prepared by drop-casting. Size distributions and mean sizes of the NPs were determined by

measurement of at least 200 individual NPs on a given grid using the Image J software, and fitted with Gaussian functions. The results are given as mean size (standard deviation).

The photoelectron emission spectra were recorded using a monochromatised Al K_α ($h\nu$ = 1486.6 eV) source on a ThermoScientific K-Alpha system at the CIRIMAT-Toulouse Laboratory. The X-ray spot size was about 400 μm. The pass energy was fixed at 30 eV with a step of 0.1 eV for core levels and 160 eV for surveys with a step of 1 eV. The spectrometer energy calibration was done using the Au $4f_{7/2}$ (83.9 ± 0.1 eV) and Cu $2p_{3/2}$ (932.8 ± 0.1 eV) photoelectron lines. XPS spectra were recorded in direct mode N (E_c) and the background signal was removed using the Shirley method. Data processing was performed using Avantage software. The flood gun was used to neutralize charge effects on the top surface. Calibration spectra with C 1s binding energy at 284.8 eV (±0.1 eV). Samples were prepared under argon in a glovebox, their transfer into the XPS chamber was carried out under argon. For the XPS measurements **NiCu NPs** were deposited by drop-casting the 2 mg mL^{-1} THF ink onto a glassy carbon plate electrode (SIGRADUR K) with an area of 0.08 cm^2. As the carbon plate electrode do not rotate, one drop of NAFION D-520 (5%) was added as an adhesive to prevent the material from fully detaching from the electrode due to the release of hydrogen bubbles. This electrode is integrated into the three-electrode electrochemical cell configuration described above in 0.1 M NaOH solution. After the bulk electrolysis, the electrode was conditioned in inert atmosphere to record XPS spectra.

X-Ray absorption spectra at Ni K-edge and Cu K-edge were acquired in transmission mode at the SAMBA beamline of the SOLEIL synchrotron, operating with an electron beam current of 450 mA. The incident energy was selected by a Si (200) double crystal monochromator. Incident flux was *ca.* 1×10^{10} ph s^{-1} using a beam size of 1 mm × 0.5 mm. Samples were prepared in air by diluting the corresponding powder with cellulose in a pellet (φ = 6 mm), followed by placement in the sample holder and sealing with 30 μm Kapton tape. Sample **NiCu NPs** was kept at 80 K in a N_2 LN$_2$-cryo cryostat. Energy calibration was performed concurrently for each measurement, with each reference metal foil placed in front of the second ion chamber. Incident energy was calibrated by referencing the inflection point of the corresponding metallic foil, which was 8333.0 eV for Ni and 8979.0 eV for Cu. Ni(0), NiO, Ni(OH)$_2$, Cu (0), Cu$_2$O and CuO spectra were recorded in identical conditions for comparison purposes. The final spectra were processed, normalized and fitted using the Athena and Artemis programs included in the DEMETER package.[47]

Metal contents were established by inductively coupled plasma atomic emission spectrometry (ICP-AES) performed at the "Laboratoire de Chimie de Coordination, Toulouse" in a Thermo Scientific ICAP 6300 instrument after digestion of the samples in *aqua regia*.

Attenuated total reflection infrared (ATR-IR) spectra were recorded on a PerkinElmer GX2000 spectrometer available in a glovebox, in the range of 4000–400 cm^{-1}.

All the electrochemical experiments were performed with a BioLogic SP-50 potentiostat. The 0.1 M NaOH solution was prepared using Milli-Q water. The solutions were degassed with an Ar flow prior to the electrochemical analysis. A glassy carbon rotating disk electrode GC-RDE (Ø 5 mm, 0.196 cm^2) was used as the working electrode (WE). The working electrodes were prepared by the traditional drop-casting method. Electrode preparation started from a 2 mg mL^{-1} dispersion of each nanomaterial in THF (2 mg in 1 mL of THF) under air. The RDE was rotated at 1000 rpm in order to ensure complete removal of *in situ* formed H$_2$ bubbles during catalytic turnover. A Pt wire was used as the counter electrode (CE) and a standard calomel electrode (SCE, Hg/Hg$_2$Cl$_2$, KCl sat.) as a reference electrode (RE). The potentials reported *versus* the normal hydrogen electrode were transformed as follows ($E_{NHE} = E_{SCE} + E^0_{SCE}$), where E^0_{SCE} = 0.244 V.

For each catalyst a linear sweep voltammetry (LSV) was first performed which allowed to calculate the onset overpotential, η_0, at the change of slope and the benchmarking overpotential, η_{10}, at a current density of j = −10 mA cm^{-2}. The stability of the catalysts was tested by chronopotentiometry (CP) that was carried out by applying a current density of j = −10 mA cm^{-2} over a prolonged period of time according to Jaramillo's methodology.[41]

To estimate the faradaic efficiency (FE) of hydrogen production, electrocatalysis was performed for 20 minutes using a two-compartment H-type cell with a fritted glass separator between the compartments. The CE was placed in one compartment and the WE and RE were placed in the second one together with the H$_2$ Clark electrode (Unisense). Both compartments were filled with 0.1 M NaOH solution and equipped with a stirring bar. Prior to each measurement, both compartments were purged with Ar. Unisense H$_2$-NP Clark electrode was used to measure the hydrogen evolved in the gas phase during the chronopotentiometry experiment.

To determine the electrochemically active surface area (ECSA), cyclic voltammograms were recorded using as working electrode a GC electrode dropcasted with the catalyst ink (10 μl of ink to reach a catalyst loading of 0.1 mg cm^{-2}), at various scan rates (ν = 10, 20, 40, 60, 80 and 100 mV s^{-1}) in 10 mM K$_3$[Fe(CN)$_6$] in 0.1 M NaOH as supporting electrolyte, degassed with argon. EIS measurements were performed in the frequency range 10^5 Hz–0.1 Hz, with a 10 points per decade sinusoidal amplitude set at 5 mV.

Double-layer capacitance (C_{DL})[41] was estimated by performing CV measurements with different scan rates. A non-faradaic region was chosen from the LSV (between 0.1–0.2 V), where no redox process takes place and the measured current is only due to double-layer charging. Based on this assumption, the charging current (i_c) was calculated as the product of the electrochemical double-layer capacitance (C_{DL}) by the scan rate (ν). Plotting i_c as a function of ν yields a straight line with slope equal to C_{DL}. In this way, the CVs were recorded at different scan rates (10, 25, 50, 75, 100, 250 and 500 mV s^{-1}), holding the working electrode at each potential vertex for 10 seconds prior to the next step.

Author contributions

Conflicts of interest

There are no conflicts of interest to declare.

Data availability

Most of the data of our work are present in the manuscript or in the ESI document.†

Authors are committed to provide the original/raw data if it is required.

Acknowledgements

References

1 N. S. Lewis and D. G. Nocera, *Proc. Natl. Acad. Sci. U. S. A.*, 2006, **103**, 15729–15735.

2 G. Glenk and S. Reichelstein, *Nat. Energy*, 2019, **4**, 216–222.

3 I. Staffell, D. Scamman, A. Velazquez Abad, P. Balcombe, P. E. Dodds, P. Ekins, N. Shah and K. R. Ward, *Energy Environ. Sci.*, 2019, **12**, 463–491.

4 K. Ham, S. Bae and J. Lee, *J. Energy Chem.*, 2024, **95**, 554–576.

5 F. Ustolin, N. Paltrinieri and F. Berto, *Int. J. Hydrogen Energy*, 2020, **45**, 23809–23840.

6 F. M. Sapountzi, J. M. Gracia, C. J. Weststrate, H. O. A. Fredriksson and J. W. (Hans) Niemantsverdriet, *Prog. Energy Combust. Sci.*, 2017, **58**, 1–35.

7 K. Zeng and D. Zhang, *Prog. Energy Combust. Sci.*, 2010, **36**, 307–326.

8 L. J. Titheridge and A. T. Marshall, *Int. J. Hydrogen Energy*, 2024, **49**, 518–532.

9 N. Danilovic, R. Subbaraman, D. Strmcnik, K. Chang, A. P. Paulikas, V. R. Stamenkovic and N. M. Markovic, *Angew. Chem., Int. Ed.*, 2012, **51**, 12495–12498.

10 N. Mahmood, Y. Yao, J. Zhang, L. Pan, X. Zhang and J. Zou, *Adv. Sci.*, 2018, **5**, 1700464.

11 K. Philippot and A. Roucoux (Eds), *Nanoparticles in Catalysis: Advances in Synthesis and Applications*, Wiley, 1st edn, 2021.

12 N. Lotfi and G. Barati Darband, *Int. J. Hydrogen Energy*, 2024, **70**, 301–314.

13 A. G. Oshchepkov, P. A. Simonov, O. V. Cherstiouk, R. R. Nazmutdinov, D. V. Glukhov, V. I. Zaikovskii, T. Yu. Kardash, R. I. Kvon, A. Bonnefont, A. N. Simonov, V. N. Parmon and E. R. Savinova, *Top. Catal.*, 2015, **58**, 1181–1192.

14 D. S. P. Cardoso, S. Eugénio, T. M. Silva, D. M. F. Santos, C. A. C. Sequeira and M. F. Montemor, *RSC Adv.*, 2015, **5**, 43456–43461.

15 R. Solmaz, A. Döner and G. Kardaş, *Int. J. Hydrogen Energy*, 2009, **34**, 2089–2094.

16 A. Y. Faid, A. O. Barnett, F. Seland and S. Sunde, *Electrochim. Acta*, 2021, **371**, 137837.

17 C. Wei, Y. Sun, G. G. Scherer, A. C. Fisher, M. Sherburne, J. W. Ager and Z. J. Xu, *J. Am. Chem. Soc.*, 2020, **142**, 7765–7775.

18 X. Zhang, J. Wang, J. Wang, J. Wang, C. Wang and C. Lu, *J. Phys. Chem. Lett.*, 2021, **12**, 11135–11142.

19 M. A. Ahsan, A. R. Puente Santiago, Y. Hong, N. Zhang, M. Cano, E. Rodriguez-Castellon, L. Echegoyen, S. T. Sreenivasan and J. C. Noveron, *J. Am. Chem. Soc.*, 2020, **142**, 14688–14701.

20 N. Romero, M. R. Axet and K. Philippot, in *Advances in Catalysis*, Elsevier, 2023, vol. 72, pp. 115–158.

21 C. Amiens, D. Ciuculescu-Pradines and K. Philippot, *Coord. Chem. Rev.*, 2016, **308**, 409–432.

22 M. R. Axet and K. Philippot, in *Nanoparticles in Catalysis*, ed. K. Philippot and A. Roucoux, Wiley, 1st edn, 2021, pp. 73–97.

23 G. Martí, Á. Lozano-Roche, N. Romero, L. Francàs, K. Philippot, R. Bofill, J. García-Antón and X. Sala, *Surface Functionalized Metal Catalysts*, 2024, pp. 105–132.

24 K. Pelzer, B. Laleu, F. Lefebvre, K. Philippot, B. Chaudret, J. P. Candy and J. M. Basset, *Chem. Mater.*, 2004, **16**, 4937–4941.

25 T. Galeandro-Diamant, I. Suleimanov, L. Veyre, M. Bousquié, V. Meille and C. Thieuleux, *Catal. Sci. Technol.*, 2019, **9**, 1555–1558.

26 K. Tatsumura, T. Watanabe, K. Hara, T. Hoshino and I. Ohdomari, *Phys. Rev. B:Condens. Matter Mater. Phys.*, 2001, **64**, 115406.

27 K. Pelzer, J. P. Candy, G. Bergeret and J. M. Basset, *Eur. Phys. J. D*, 2007, **43**, 197–200.

28 K. Pelzer, M. Hävecker and M. Boualleg, *Angew. Chem.*, 2011, **123**, 5276–5279.

29 M. Yousuf, P. C. Sahu, H. K. Jajoo, S. Rajagopalan and K. G. Rajan, *J. Phys. F: Met. Phys.*, 1986, **16**, 373–380.

30 B. Huang, H. Kobayashi, T. Yamamoto, T. Toriyama, S. Matsumura, Y. Nishida, K. Sato, K. Nagaoka, M. Haneda, W. Xie, Y. Nanba, M. Koyama, F. Wang, S. Kawaguchi, Y. Kubota and H. Kitagawa, *Angew. Chem., Int. Ed.*, 2019, **58**, 2230–2235.

31 H. Nosé, *J. Phys. Soc. Jpn.*, 1961, **16**, 342–342.

32 M. C. Biesinger, B. P. Payne, A. P. Grosvenor, L. W. M. Lau, A. R. Gerson and R. St. C. Smart, *Appl. Surf. Sci.*, 2011, **257**, 2717–2730.

33 M. C. Biesinger, *Surf. Interface Anal.*, 2017, **49**, 1325–1334.

34 X. Xu, J. Zhang, L. Zhang, H. Huang, C. Fu, Y. Cheng and C. Niu, *J. Alloys Compd.*, 2021, **858**, 157711.

35 P. J. Grunthaner, F. J. Grunthaner and A. Madhukar, *J. Vac. Sci. Technol.*, 1982, **20**, 680–683.

36 H. Chen, D. Ge, J. Chen, R. Li, X. Zhang, T. Yu, Y. Wang and S. Song, *Chem. Commun.*, 2020, **56**, 10529–10532.

37 T. Yano, M. Ebizuka, S. Shibata and M. Yamane, *J. Electron Spectrosc. Relat. Phenom.*, 2003, **131–132**, 133–144.

38 J. E. S. Van Der Hoeven, J. Jelic, L. A. Olthof, G. Totarella, R. J. A. Van Dijk-Moes, J.-M. Krafft, C. Louis, F. Studt, A. Van Blaaderen and P. E. De Jongh, *Nat. Mater.*, 2021, **20**, 1216–1220.

39 C. Cerezo-Navarrete, Y. Mathieu, M. Puche, C. Morales, P. Concepción, L. M. Martínez-Prieto and A. Corma, *Catal. Sci. Technol.*, 2021, **11**, 494–505.

40 L. Zhang, H. Hu, C. Sun, D. Xiao, H.-T. Wang, Y. Xiao, S. Zhao, K. H. Chen, W.-X. Lin, Y.-C. Shao, X. Wang, C.-W. Pao and L. Han, *Nat. Commun.*, 2024, **15**, 7179.

41 C. C. L. McCrory, S. Jung, I. M. Ferrer, S. M. Chatman, J. C. Peters and T. F. Jaramillo, *J. Am. Chem. Soc.*, 2015, **137**, 4347–4357.

42 A. Morozan, H. Johnson, C. Roiron, G. Genay, D. Aldakov, A. Ghedjatti, C. T. Nguyen, P. D. Tran, S. Kinge and V. Artero, *ACS Catal.*, 2020, **10**, 14336–14348.

43 B. Brunetti, E. De Giglio, D. Cafagna and E. Desimoni, *Surf. Interface Anal.*, 2012, **44**, 491–496.

44 S. Anantharaj, S. Noda, M. Driess and P. W. Menezes, *ACS Energy Lett.*, 2021, **6**, 1607–1611.

45 T. Shinagawa, A. T. Garcia-Esparza and K. Takanabe, *Sci. Rep.*, 2015, **5**, 13801.

46 D. S. Hall, C. Bock and B. R. MacDougall, *J. Electrochem. Soc.*, 2013, **160**, F235–F243.

47 B. Ravel and M. Newville, *J. Synchrotron Radiat.*, 2005, **12**, 537–541.